ELSEVIER

Contents lists available at ScienceDirect

Materials Science & Engineering A

journal homepage: www.elsevier.com/locate/msea



The LPBF printability and as-printed mechanical properties of a Ti6246 alloy as a function of printing parameters and microstructure

Thibault Mouret D, Aurore Leclercq, Vladimir Brailovski D

Department of Mechanical Engineering, École de technologie supérieure, Montreal, QC, H3C 1K3, Canada

ARTICLE INFO

Keywords: Additive manufacturing Laser powder bed fusion Titanium alloy Microstructural evolution Mechanical properties

ABSTRACT

Laser Powder Bed Fusion (LPBF) of titanium alloys has been widely investigated in the last decades and introduced in industry with concrete applications. Recently, the literature has highlighted the printability of various titanium alloys with different elemental compositions. Among them, a highly resilient Ti-6Al-2Sn-4Zr-6Mo alloy (Ti6246) was identified as a promising material for the automotive and aerospace industries, and the results of its successful printing using high-power systems ($P_{\text{max}} = 400 \text{ W}$) have already been reported. In the present work, Ti6246 alloy was printed on a power-limited system ($P_{\text{max}} = 200 \text{ W}$) using fifty-three printing parameter sets with variations in terms of laser power, scanning speed and hatching space, keeping the layer thickness constant at 50 µm. The as-built samples were then characterized to correlate the printing parameters to the microstructure, phases and mechanical properties. The results revealed that a volumetric energy density of ~100 J/mm³ combined with a hatching space of ${\sim}150~\mu m$ was necessary to produce highly dense (>99.9 %) samples with a reduced number of processing-induced flaws (keyhole pores and lack-of-fusion defects) and with homogeneous microstructure. These samples manifested excellent mechanical resistance and hardness (UCS >1000 MPa and HV > 450 HV0.3), but a very limited ductility, thus indicating the need for subsequent post-processing. Using printing parameters corresponding to the highest energy input (135 J/mm³) resulted in a partial in-situ $\alpha'' \to \alpha$ $+ \beta$ phase transformation. This phenomenon was attributed to a significant overlap between two subsequently melted tracks, which reduced the cooling rate in the solidified material and promoted the formation of stable α and β phases of titanium. This latter observation provided useful insight into the printing of functionally graded Ti6246 parts.

1. Introduction

In the past decades, the aerospace, automotive and biomedical industries contributed significantly to the development of additive manufacturing (AM) processes, benefiting from their numerous advantages over conventional manufacturing techniques [1,2]. These disruptive technologies are especially interesting as they are versatile, agile and enable to print complex and intricate geometries with great accuracy, especially for small production lots that are not economically viable with conventional processes. AM processes are generally based on the sequential layer-by-layer build principle, and thus allow the near net shape manufacturing. As a result, the wastes generated during printing and the machining allowances needed to obtain final geometries are greatly reduced, thus decreasing the buy-to-fly ratio, and therefore, the cradle-to-gate environmental footprint. The well-known agility of AM processes facilitates their direct on-demand deployment, thus enhancing

the efficiency of the supply chain and minimizing production downtime caused by the need for replacement of worn parts.

Among AM processes, laser powder bed fusion (LPBF) emerges as the best-suited for the production of small-to-medium size parts, since fine powdered feedstocks (20–50 μ m) used in the process and narrow melt pools (50–200 μ m) generated by the laser beam enable to print parts with resolutions as small as 0.1–0.2 mm at a lower cost than its principal competitors (electron beam powder bed fusion (EB-PBF) or directed energy deposition (DED)) [3]. During the last two decades, LPBF has been extensively implemented, and numerous printing parameter sets and varieties of printing equipment made available, covering almost all the families of metallic materials, including iron- [4], nickel- [5], aluminum- [6] and even refractory [7] alloys. As far as the titanium alloys are concerned, LPBF has demonstrated its suitability to print most of them, providing the process parameters are adapted to the physical and chemical properties of the alloys. Among newer printable titanium

E-mail address: vladimir.brailovski@etsmtl.ca (V. Brailovski).

https://doi.org/10.1016/j.msea.2025.149061

^{*} Corresponding author.

alloys, titanium aluminide γ -TiAl [8] and orthorhombic Ti₂AlNb alloy [9], deserve special mention since they offer an excellent combination of service properties. This notwithstanding, titanium alloys having only a small percent of elemental additions, and more specifically Ti-6Al-4V (hereafter referred as Ti64), are undoubtedly among the most studied LPBF-ready metallic materials [10,11]. Because of its exceptional strength-to-weight ratio (>180 MPa/(g.cm $^{-3}$) [12,13]), Ti64 was initially developed primarily for aerospace applications (since the mid-1950s), but was ultimately also adopted as a biomedical implant material due to its excellent corrosion resistance and decent biocompatibility [14,15].

The mechanical properties of conventional titanium alloys can be tailored to suit specific application requirements via the adjustment of their phase composition and microstructure. Depending on the chemical composition, at temperatures close to room temperature, α (hexagonal close-packed (HCP)), β (body centered cubic (BCC)) or a mixture of both crystallographic phases can generally be found [16]. The alloying elements play a fundamental role in the alloys' phase composition as they act as either α (e.g., Al, N, O, Zr) or β (e.g., Fe, V, Mo, Nb) stabilizers [17]. Alpha and near- α titanium alloys, such as Ti-3Al-2.5V (Grade 9) or Ti-5.5Al-3.5Sn-3Zr-1Nb (IMI 829), are especially interesting for the petrochemical industry because of their excellent weldability, high oxidation and corrosion resistance at elevated temperatures, and the highest strength in these conditions [18]. However, their modest room temperature mechanical properties, combined with poor workability, make them considerably less noteworthy. Furthermore, as single phase alloys, their mechanical properties cannot be improved by controlled heat treatment, but only using thermomechanical processing, which is significantly more expensive [19]. In this context, $\alpha + \beta$, near- β or β alloys with varying proportions of β stabilizers have been developed to improve both the strength and workability of these multiphase materials via the appropriate heat treatments [20,21]. The ability of titanium alloys to retain a significantly high β content in the 20–900 °C temperature range is characterized by the beta-stability index (SI_{β}) [22–24]. This index is calculated using equation (1), where [Mo]EO and [Al]EO correspond respectively to the equivalent molybdenum (2) and aluminum (3) concentrations, and the higher the value of this index, the greater the alloy's propensity to retain β phase after quenching from the temperatures above the beta transus.

$$SI_{\beta} = [Mo]_{EQ} - [Al]_{EQ} (wt\%)$$
 (1)

$$[Al]_{FO} = [Al] + \frac{1}{3}[Sn] + \frac{1}{6}[Zr] + 10([C] + [O] + 2[N])$$
(3)

Among duplex $(\alpha+\beta)$ alloys, Ti-6Al-2Sn-4Zr-6Mo (hereafter called Ti6246) stands out and it is currently used to produce such parts as compressor disks and blades for turbine engines. Ti6246 provides excellent elevated temperature mechanical properties, such as YS = 935 MPa [25], as compared to 755 MPa for Ti64 [26], both at 400 °C. Sometimes, Ti6246 is even considered a near- β titanium alloy as it is prone to retaining a greater fraction of β phase (SI $_{\beta}=-1.33$) compared to other $\alpha+\beta$ alloys, including Ti64 (SI $_{\beta}=-3.33$). In addition to its excellent strength, Ti6246 demonstrates a good oxidation resistance at moderate temperatures by forming a rutile TiO $_2$ layer on the surface [27, 28], as well as a great corrosion resistance in diverse environments thanks to its high molybdenum content [29,30].

One of the specific and interesting features of Ti6246 alloys processed by LPBF is the formation of metastable martensite

microstructures which differ from those obtained for the majority of titanium alloys. For example, in the majority of duplex $(\alpha+\beta)$ alloys, such as Ti64, rapid cooling $(\sim 10^6-10^8~{\rm C/s})$ inherent to the LPBF process induces the formation of hexagonal α' martensite [31]. On the contrary, for alloys with a higher β stabilizers content, such as Ti6246, the resulting martensite generally has an orthorhombic crystallographic structure (α'') [32,33]. In both cases, however, the as-built LPBF titanium alloys need to be annealed to transform the metastable microstructures into their stable counterparts, thus improving the mechanical properties.

Although significantly less known than Ti64, Ti6246 has been recently studied to produce parts using the LPBF process. Carrozza et al. were the first to compare the LPBF printability and post-processing of this alloy with the reference Ti64 alloy [34–36]. The authors produced high density (\geq 99 %) Ti6246 parts with significantly higher mechanical properties than those of their LPBF Ti64 counterparts, and even the wrought Ti6246 alloy [37]. Their best compromise in terms of strength, hardness and ductility was achieved with a bi-lamellar α microstructure after annealing at 875 °C for 1h. Additional publications of this research group revealed the results of optimizing the solution and aging post-treatment treatments to further tailor the microstructure and obtain the best compromise in terms of tensile strength and ductility at room temperature [38]. Some other studies demonstrated the possibility of achieving ultra-high hardness characteristics (≈600 HV) in this alloy [39,40] via the formation of nano-sized α laths resulting from the application of specific process and post-process conditions [41]. Kan et al. revealed that the nanocrystalline microstructure and the associated high hardness obtained for the heat-treated LPBF Ti6246 alloy enable to obtain samples which display remarkable wear resistance as compared to Ti64 (either conventionally manufactured or 3D-printed) [42]. Recently, some publications were focused on the corrosion resistance of LPBF Ti6246 specimens to such species as H₂S, CO₂, NaCl, NaF, etc. [43, 44]. Nonetheless, to the best of the authors' knowledge, no comprehensive study comparing the microstructure and the as-built mechanical properties of a Ti6246 alloy for different LPBF parameter sets has yet been published.

To complement the existing body of knowledge, this study explores the basic printability of the Ti6246 alloy. To this end, a wide range of printing parameters was explored in a bid to correlate the printing conditions with the structural, physical and mechanical characteristics of printed Ti6246 parts and compare them with the literature data.

2. Material and methods

2.1. Powder characterization

The Ti-6Al-2Sn4Zr-6Mo powder used in this study is a gas-atomized pre-alloyed powder provided by Eckart TLS GmbH. According to the supplier, the nominal composition of the powder fulfils the composition requirement of the AMS 4981 standard [45], with low amounts of impurities (O, N, C, H < 0.15 %wt). The particle size distribution of D10 = 26, D50 = 43 and D90 = 64 (µm) was measured using the water module of an LS13 320 XR particle size analyzer (Beckman Coulter, Brea, CA, USA) (Fig. 1a). The particle morphology was then observed using a TM3000 scanning electron microscope (SEM) (Hitachi, Tokyo, Japan), (Fig. 1b).

2.2. Plan of experiments

The printer used in this study was a TruPrint 1000 system (TRUMPF GmbH, Ditzingen, Germany), with the laser power (P) varying from 20 to 200 W and the scanning speed (ν) varying from 20 to 3000 mm/s. Based on the particle size distribution analysis (Section 2.1), the layer

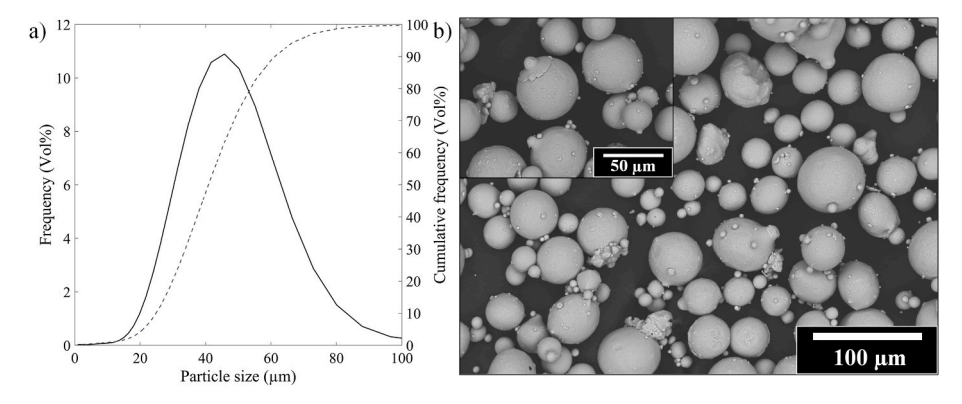


Fig. 1. Ti6246 powder: a) Particle size distribution and b) SEM observations.

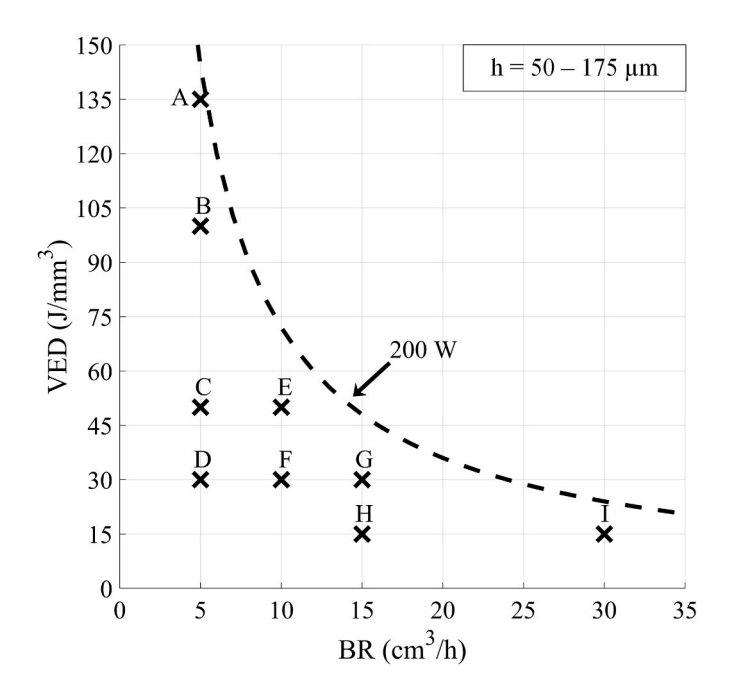


Fig. 2. 2D Representation of the nine VED-BR experimentally printed parameter sets; the dashed line represents the VED-BR limit corresponding to a maximal laser power of 200 W.

thickness (t) was set at 50 μ m (\sim 0.8*D90) and kept constant over course of the study. This layer thickness prevents mechanical sieving of powders during recoating, which could decrease the density of the powder bed. In order to study the impact of a wide range of process parameters on the density, structure and mechanical properties of printed specimens, 9 different sets of printing parameters (A, B, C, D, E, F, G, H, I)

were selected in the VED (4) - BR (5) space (Fig. 2):

$$VED\left(J/mm^3\right) = \frac{P}{vht} \tag{4}$$

$$BR(cm^3/h) = vht (5)$$

where VED (J/mm^3) is the volumetric energy density; BR (cm^3/n) is the build rate and h (μm) is the hatching space.

Each of the 9 sets of printing parameters corresponds to one of the 6 hatching space (h) values ranging incrementally as 50, 75, 100, 125, 150 and 175 μ m. Each parameter set is named using the corresponding letter and hatching space value. For example, D-100 stands for parameter set D with hatching space $h=100~\mu$ m. Note that because of speed limitations (v<3000~mm/s), it was not possible to use parameter set I with the smallest hatching space value of $h=50~\mu$ m. Overall, the plan of experiments represents a total of 9*6-1 = 53 different parameter combinations (Table 1).

Using this plan of experiments, fifty-three 4.5 mm-long single tracks and 10 mm-diameter, 20 mm-high cylindrical specimens corresponding to each of the process parameter sets were printed on a Ti64 baseplate without preheating. The single tracks (Fig. 3a), spaced at 1 mm intervals, were printed on the upper surface of three 10x15x15 (mm) rectangular specimens (Fig. 3b). The cylindrical specimens were printed (Fig. 3c) and then removed from the baseplate, their supports cut off, and remaining parts partitioned to obtain samples for structural analyses, microhardness measurements, micro-computed X-ray tomography (μ -CT), and compression testing (Fig. 3d).

2.3. Physical and structural characterization

2.3.1. Single track measurements

The single tracks were analyzed using high magnification (x200) stitched images obtained with a Keyence VHX7000 optical microscope $\frac{1}{2}$

Table 1Plan of experiments in terms of the laser power (P), scanning speed (v) and hatching space (h) values used for each of the nine parameter sets.

Set	VED (J/mm ³)	BR (cm ^{3/} h)	P (W)			h (µ	ım)		
				50	75	100	125	150	175
						ν (mi	m/s)		
A	135	5	188	557	370	278	222	185	159
В	100		139						
C	50		69						
D	30		42						
E	50	10	139	1111	741	556	444	370	317
F	30		83						
G	30	15	125	1667	1111	833	667	556	476
H	15		63						
I	15	30	125	/	2222	1667	1333	1111	952

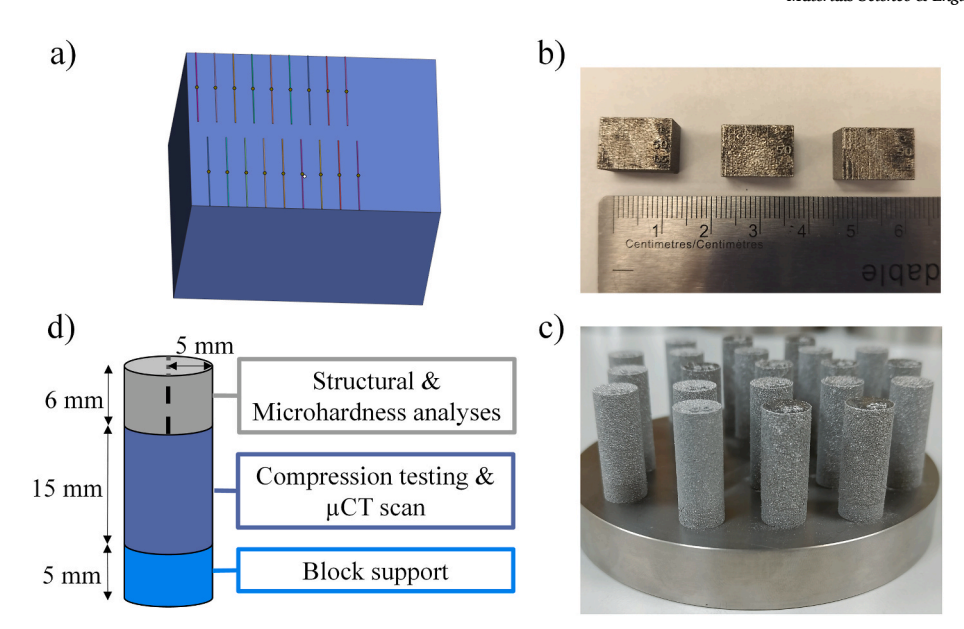


Fig. 3. a) Drawing of one of the cubic samples with 18 single tracks; b) photo of three cubic samples with single tracks; c) photo of a baseplate with printed cylindrical specimens; d) schematic representation of the cylindrical specimen with samples used for various analyses.

(Osaka, Japan). Ten profile lines were drawn perpendicular to each of the tracks to measure their average widths and corresponding standard deviations.

2.3.2. Density measurements

The level of porosity in the 53 printed samples (Table 1) was assessed using micro-computed tomography (μ CT) scans of their 15 mm-long parts (analyzed volume $\approx 1000~\text{mm}^3$) (Fig. 3d). These parts were later used for compression testing. Multiple studies have highlighted the pertinence of using μ CT as the density measurement technique for LPBF parts [46]. In comparison to alternative methods such as the Archimedes' technique and microscopy, μ CT offers the distinct advantage of providing 3D information of the pore network (pore size, roundness, location, etc.)

The μCT analyses were performed using an FF35 CT system (Comet Yxlon, Germany). Given the large number of scans needed to inspect the 53 samples, a compromise between the acquisition time and scan quality was found, resulting in 1500 projections with an X-ray tube voltage of 140 kV, a tube current of 50 μA , and an exposure time of 475 ms over 3 frames integration. To limit the beam hardening effect, a 0.3 mm copper filter was used. The projection data were then corrected and reconstructed using the Siemens CERA software, with a resulting voxel size of 8 μm .

The porosity analyses were realized using the Dragonfly software (Comet Technologies, Canada). The pores were isolated through the manual adjustment of a grey-level threshold and the volume of a segmented region of interest was related to the overall volume of each individual sample to determine the printed density. To obtain statistical information regarding the pore size and shape distributions, the connectivity of voxels corresponding to each individual pore was assessed considering 6-connected components (faces), and pores smaller than $3 \times 3 \times 3$ voxels ($<1.4*10^{-5} \, \mu m^3$) in size were removed from the dataset. The pore volume (V_p) was computed considering the number of connected voxels in each isolated pore, while the pore sphericity (S) was calculated using equation (6).

$$S = \frac{\left(6\pi^{1/2}V_p\right)^{\frac{2}{3}}}{A_p} \tag{6}$$

where V_p is the pore volume and A_p the surface area of the pores estimated using Lindblad surface area method [47].

2.3.3. Microstructure and phase analyses

The microstructure and phase analyses were performed on Z-Y cross-sections of the distant parts of the printed samples (Fig. 3d). The crystallographic phases were identified by X-ray Diffraction (XRD), using an X'Pert3 system (Malvern Panalytical Ltd, Malvern, UK) equipped with a cobalt source (K_{α} Co = 1.79026 Å). The acquisitions were made in the Bragg Brentano configuration, with a step size of 0.017° and a 2θ range between 38 and 50°. This reduced 2θ range encompasses the main reflections of all the expected phases (α '', α ', α , β).

For in-depth microstructural observations, the Z-Y cross-sections of the samples for each parameter set were mounted in carbon-dopped resin, mirror polished and etched (1 min) with a Kroll reagent (%vol: 2:5:93 HF/HNO₃/H₂O). Observations were performed at two distinct scales. A lower-resolution overview was carried out using a LEXT OLS4100 (Lext Olympus Corp., Japan) confocal microscope with the lowest magnification (x5). The columnar microstructure, some grain boundaries and especially crystallographic inhomogeneity were observed using this equipment. To observe finer microstructure features, including martensite laths formed in the as-built samples, higher magnification images were captured using a secondary electron detector (acceleration voltage 10 kV, magnification 30k) of an SU-8230 Field Emission STEM (Hitachi, Tokyo, Japan), and the average width of the lath structures was measured using the ImageJ software. The homogeneity of the microstructure was asserted by repeating the measurements on ten images randomly acquired over each area of interest.

2.4. Mechanical characterization

2.4.1. Microhardness

Microhardness measurements were performed on the etched Y-Z cross-sections using a Duramin-40 M1 measurement system (Struers, Ballerup, Denmark). To prevent measurement variations caused by the presence of pores on planar cross-sections, only samples having a measured density higher than 95 % were considered. For all of them, 10 measurements were performed in the middle of the samples with an applied force of 300 gF and a dwell time of 15 s. In addition, when phase inhomogeneities were revealed after etching, additional series of 10 microhardness measurements were carried out on these specific regions, using the same measurement conditions.

2.4.2. Compression testing

The middle part of each of the printed specimens (Fig. 3d) was subjected to room-temperature compression testing using an Alliance RF/200 mechanical testing system (MTS, Eden Prairie, MN, USA) following the E9-09 ASTM standard [48]. The compression rate was set at 0.01 mm/s and a video camera coupled with a microphone was placed in front of the specimens. A 200 kN MTS load cell measured the force, while the displacement was measured using an LVDT. From these measurements, compression strain-stress diagrams were plotted and audio spectra recorded, to compare the onset of cracking with the inflexion points observed on the stress-strain diagrams. This step was necessary since the compression testing mode allowed to accommodate cracks and continue testing, especially when samples were porous or contained unmelted particles, resulting in significant overestimations of both the apparent material strength and ductility. The following metrics were extracted from the compression testing: the Ultimate Compression Strength (UCS, MPa), defined as the maximum stress reached during the test; the Yield Strength (YS, MPa), calculated by moving the slope from origin to 0.2 % on the strain axis, and the Strain to failure $(\delta, \%)$.

3. Results

3.1. Single tracks

The optical measurements of single tracks allowed to assess their average widths (W) and classify them into three distinct groups, namely, continuous (Fig. 4a), irregular (Fig. 4b) and partially fused (Fig. 4c). The width of the continuous tracks ranged from 85 to 400 μ m and that of the irregular or partially fused tracks ranged from 65 to 150 μ m (Table 2). A direct correlation was observed between the track quality and the linear energy density of the laser (LED, (7)) used to melt the powder bed (Fig. 4d).

$$LED(J/mm) = \frac{P}{\nu} \tag{7}$$

Based on these observations, two distinct process parameter-related threshold values were established. In the case of scanning speeds exceeding 550 mm/s, most of the single tracks were categorized as irregular or partially fused, and the higher the scanning speed, the greater the track non-uniformity, and the smaller the single track widths (Fig. 4d). The appearance of the irregular and partially fused tracks may also be related to $LED \leq 0.2$ J/m. In both cases, the energy input delivered to the powder bed was insufficient, leading to the appearance of unmelted areas along the scanning tracks or to tracks with important

discontinuities, and width and thickness variations. This behavior concerned mainly the parameter sets with low *LED* values, such as those using low laser powers (*P*) (*e.g.*, sets D, F, H) or those with higher powers (*P*), but with much greater scanning speeds (ν) (*e.g.*, sets G, I). The formation of continuous and uniform single tracks corresponds to the A, B, C and E printing parameter sets with $\nu \le 550$ mm/s and $LED \ge 0.2$ J/m.

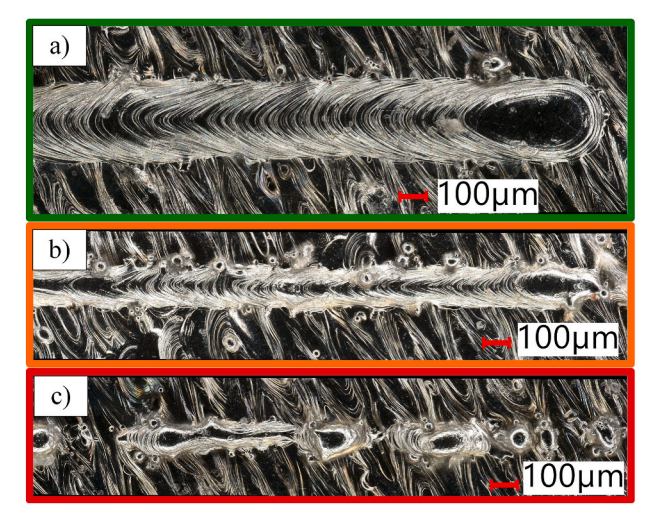
3.2. Printed density

All the parameter sets mentioned in Table 1 allowed to successfully print cylindrical specimens, even if the associated single tracks were irregular or partially fused. The use of X-ray micro-computed tomography allowed to conclude that all the printed samples were crack-free, regardless of the printing parameters used. The as-printed densities obtained from the CT-scans of each of the printed specimens are summarized in the appendix (Table A.1). To highlight the correlations between printed densities and printing parameters, the density values were plotted in the 3D *VED-BR-h* space in Fig. 5. Using this representation, it was determined that a minimum *VED* of 50 J/mm³ was required to achieve a printed density greater than 95 %; to reach a density greater than 99 %, the *VED* had to be greater than 100 J/mm³.

In addition to higher *VED*, these results showed the benefits using greater hatching spaces h, *i.e.*, lower scanning speeds ν , to improve the overall printed densities. This behavior was especially evident in sets exhibiting a broad range of densities (*e.g.*, D, F, G). These observations are consistent with the results of quality analysis of the corresponding single tracks. The parameter set B had the smallest number of defects (density systematically greater than 99.9 %) and was found to be less sensitive to the hatching space (h) and scanning speed (ν) variations.

To illustrate the influence of *VED* ranging from 50 to 135 J/mm³ on the processing-induced porosity, Fig. 6a,b,c summarizes the segmented pores inside the 15 mm high cylindrical samples (Fig. 3d). Differences in terms of the porosity characteristics are visible above and below the optimized parameter set B ($VED = 100 \text{ J/mm}^3$) (Fig. 6b). For the highest energy input (set A, Fig. 6a, $VED = 135 \text{ J/mm}^3$), the segmented pores are mainly small and circular (Fig. 6d), while for the lower energy inputs (set E, Fig. 6c, $VED = 50 \text{ J/mm}^3$), pores are larger and manifest non-uniform shapes (Fig. 6e). In the highly porous samples ($VED \le 30 \text{ J/mm}^3$, non-shown in the figure), pores of several dozens of mm³ in size form an extended and interconnected pore network.

The pore volume and sphericity distributions for the *VED* ranging from 50 to 135 J/mm³ are shown in Fig. 6f,g. These statistical analyses confirm that samples printed with the highest *VED* (set A) contain a high proportion of small keyhole pores ($V_p < 1e^{-5} \mu m³$) with a high sphericity



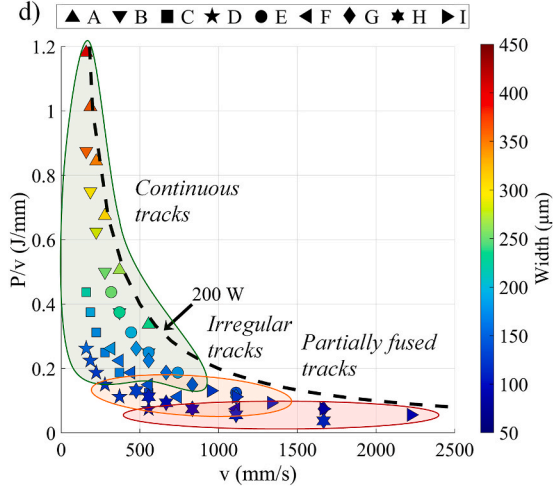


Fig. 4. Optical observations of the a) continuous, b) irregular and c) partially fused single tracks; d) single track widths according to the scanning speed v and the linear energy density P/v.

Laser power (P), scanning speed (v) and single-track width (W) for each of the nine parameter sets.

Set	P (W)	h (µm)											
		50		75		100		125		150		175	
		v (mm/s)	W (µm)	v (mm/s)	W (µm)	ν (mm/s)	W (µm)	$\nu (\text{mm/s})$	W (µm)	v (mm/s)	W (µm)	v (mm/s)	W (µm)
A	188	257	$235{\pm}19$	370	266±17	278	306 ± 25	222	348±22	185	366 ± 15	159	404±25
В	139		$192{\pm}16$		222 ± 14		253 ± 21		284 ± 13		297 ± 11		360 ± 26
O	69		$125{\pm}11$		165 ± 11		165 ± 11		171 ± 12		189 ± 9		220 ± 9
D	42		$86{\pm}19$		120 ± 12		119 ± 15		123 ± 15		137 ± 7		150 ± 18
ы	139	1111	134 ± 15	741	175 ± 24	556	175 ± 14	444	194 ± 16	370	231 ± 15	317	251 ± 28
щ	83		$99{\pm}16$		138 ± 16		137 ± 13		145 ± 7		154 ± 15		178 ± 12
G	125	1667	$101{\pm}14$	1111	149 ± 13	833	139 ± 17	299	152 ± 18	556	164 ± 10	476	176 ± 6
Н	63		$113{\pm}22$		108 ± 23		91 ± 12		94 ± 14		104 ± 16		125 ± 16
I	125	\	\	2222	99 ± 11	1667	91 ± 12	1333	112 ± 14	1111	118 ± 16	952	121 ± 12

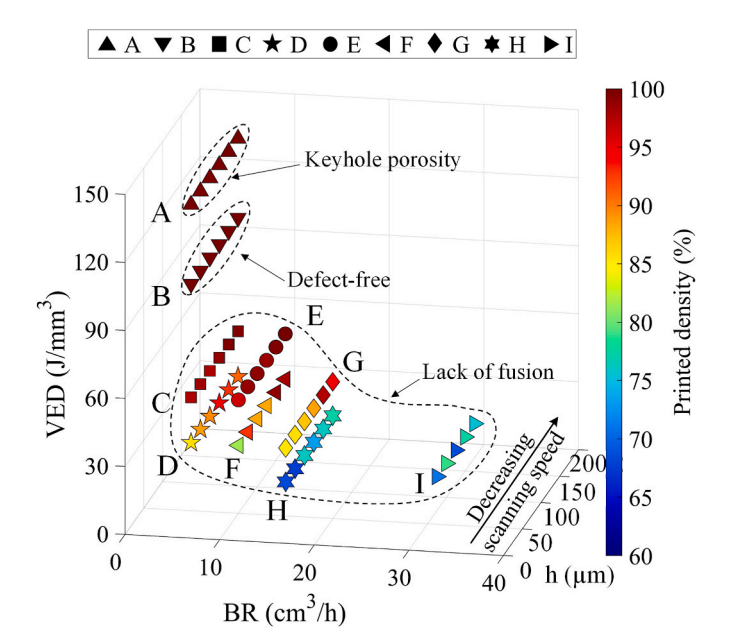


Fig. 5. CT-scan measured density in the VED-BR-h space, with different types of porosities encircled.

(*S* close to 1). On the other hand, the B-set samples manifest a very limited number of larger pores with a comparably high sphericity as the A-set samples. Finally, the E-set samples contain numerous lower-sphericity defects (lack-of-fusion) with a broader volume distribution.

Optical observations made on the samples printed using the highest *VED* (set A, Fig. 7a) attest the presence of small and circular keyhole pores. The round shape and position of these pores at the bottom of melt pools are typical for this kind of defects. Conversely, in highly porous samples, the porosities observed are wider and have highly irregular shapes (set E, Fig. 7b), which is characteristic of lack-of-fusion defects.

3.3. Phases and microstructure

The X-ray diffractograms for varying VED values (parameter sets A to H) with the smallest hatching space h (50 μ m) are plotted in Fig. 8a, whereas for the highest VED-BR set A with the h values varying from 50 to $175 \mu m$, they are plotted in Fig. 8b. It can be observed that most of the samples (B-H with $h = 50 \mu m$) are indexed as containing orthorhombic martensite (α "), which was also detected in the powder feedstock. The orthorhombic martensite was expected in this titanium alloy, both in the powder and solid forms, given the significant level of β stabilizers and rapid cooling in both cases: up to 108 K/s during plasma atomization process and in the range of 10^4 – 10^6 K/s during LPBF. However, for some specific printing parameters, especially those with high VED (set A) and low hatching space h, and therefore, high scanning speeds, the X-ray diffractograms (Fig. 8b) suggested the presence of mixed α/α (HCP) – β (BCC) microstructures. These phases are distinguished by their distinct peaks in the 44-48° 2θ range which are shifted compared to those of orthorhombic α " martensite. Note that the XRD analysis does not allow to distinguish between α and α' phases as they both have the same hexagonal crystalline structure.

The observations of the etched surfaces made with a confocal microscope enabled to detect the feature characteristics of the various phases present in the material. Fig. 9a corresponds to the completely α '' martensitic structure (B-150) which is a common reference phase in LPBF-processed titanium alloys with a high β stabilizers content. Conversely, a non-uniform microstructure was also observed in some samples (e.g., A-50, Fig. 9b). In the upper part of these samples, a wide bright martensite α '' layer that almost did not react with the Kroll reagent was systematically observed, while their remaining part was

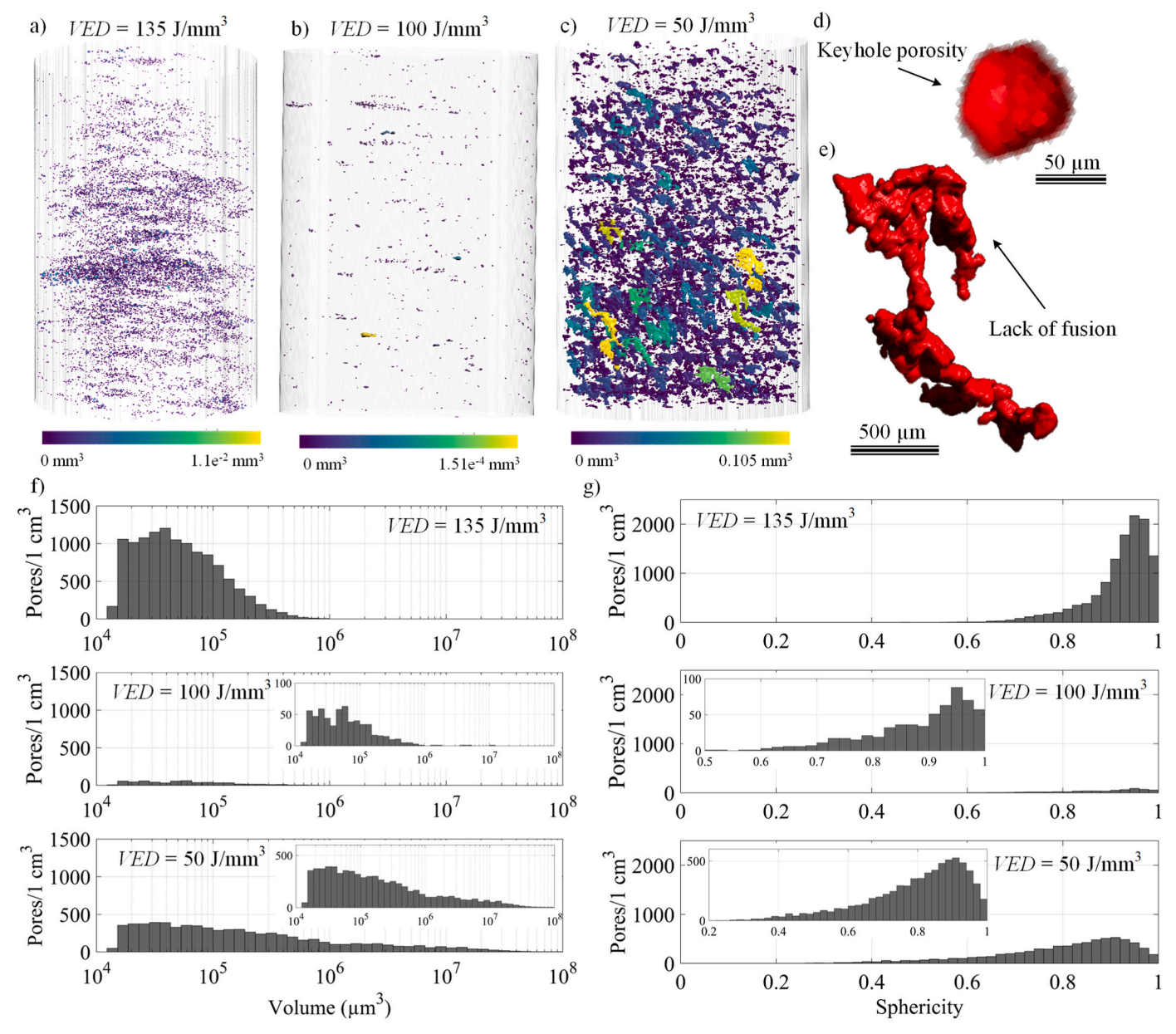


Fig. 6. Examples of the porosity distributions inside the 15 mm-high cylindrical specimens printed at different VED: a) 135 J/mm³ A-50; b) 100 J/mm³ B-150; c) 50 J/mm³ E-100; 3D segmented process-induced flaws: d) a keyhole pore (A-50) and e) a lack-of-fusion defect (E-50); Pore distributions for different VED: f) volume; g) sphericity.

brown-colored due to the presence of β phase. Note that the B-set samples printed with small h values (e.g., B-50), reveal slight traces of in situ transformation (brown areas) which cannot be found in the B-set samples with higher h values (e.g., B-150). Using such printing parameters enable to print samples with a homogeneous as-built microstructure.

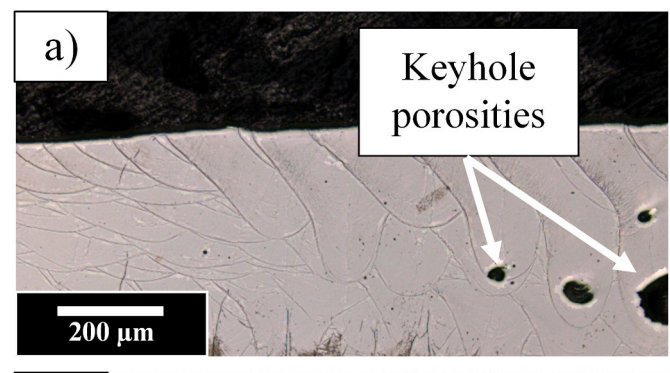
The optical images taken at higher magnifications allowed to detect differences between the two competing microstructures. In fully martensitic samples (Fig. 9a) or inside the bright upper layers (Fig. 9b) of the heterogenous samples, the melt pool borders and a few typical columnar prior- β grains were observed (Fig. 9c). In the brown area of the heterogeneous samples (Fig. 9d), wide columnar β grains and their borders were identified (Fig. 9d). Thin elongated needles characteristic of the martensitic microstructure of titanium alloys could be observed using high magnification SEM images. Needles of orthorhombic α ' martensite were bright (Fig. 9e), while those of hexagonal α ' martensite were dark (see Fig. 9f), but both types were arranged in a \pm 90 fashion.

Note that the thickness of the observed α '' layer increased with an increase in the hatching space h, i.e., with a decrease in the scanning speed (Fig. 10a). Next, according to the high-resolution SEM image measurements, the larger the hatching space h, i.e., the lower the scanning speed, the thinner the α' martensite needles (width decreases from \sim 50 to 20 nm) and the thicker the α' ' needles (width increases from \sim 50 to 60 nm (Fig. 10b)). Note also that the same microstructure heterogeneity was observed on the lateral side of some cylindrical samples, especially those directly exposed to argon flow.

3.4. Mechanical properties

3.4.1. Microhardness

The microhardness measurements were performed only on samples with densities exceeding 95 % (A, B, C and E, $VED \ge 50 \text{ J/mm}^3$, Fig. 5). In Fig. 11, a clear difference between the samples printed using higher ($\ge 100 \text{ J/mm}^3$) and lower ($\le 50 \text{ J/mm}^3$) VED can be observed. Samples



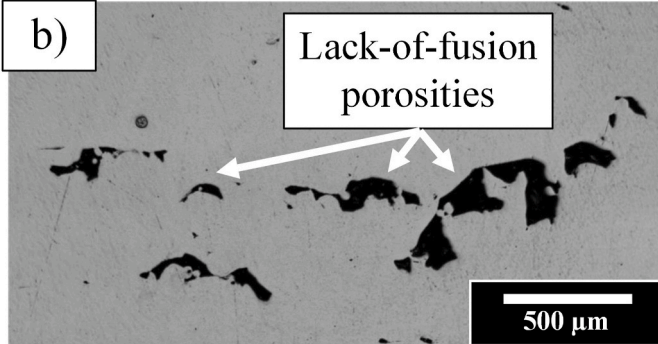


Fig. 7. Optical images of the a) keyhole porosities (A-75) and b) lack-of-fusion porosities (E-100).

with a mixture of hexagonal α' martensite and β phase (set A) exhibited higher microhardness (HV > 450) than their fully orthorhombic α 'martensite counterparts (sets B, C, E). This is in agreement with the softening-hardening phenomenon related to the presence of orthorhombic α' ' reported in Refs. [37,49]. The additional measurements realized within the α' ' martensite layers on the top of heterogeneous samples (Fig. 9b) yielded similar hardness values as those measured in their fully α' ' counterparts (Fig. 9a). No clear trend was observed with respect to the hatching space h variations.

3.4.2. Compression testing

The printed samples were subjected to compression testing at room temperature, including those with the lowest measured density. Fig. 12a presents typical stress-strain curves of the samples printed using each of the *VED* printing parameter sets. As mentioned in section 2.4.2, the curves were corrected according to audio spectra recorded to prevent

the overestimation of the material strength and ductility. The dashed lines in Fig. 12a correspond to the data recorded during the compression tests after the onset of cracking (acoustic signal). Note that the material behavior depends significantly on the *VED* values, and the higher this value, the higher the stress, but the lower the strain to failure. Fig. 12b and Fig. 12c, correspond respectively to the photo recorded at the onset of cracking, of a "brittle" sample (A-50) and of a "ductile" sample (H-50).

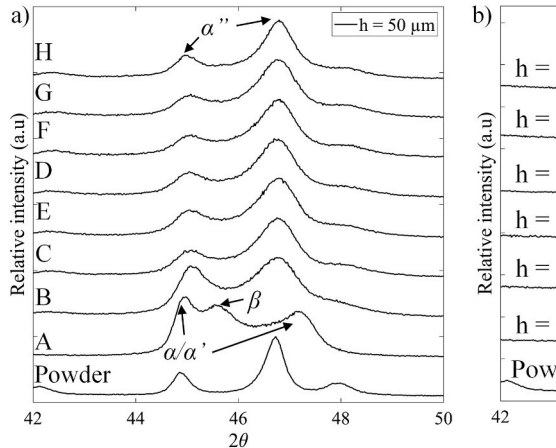
Fig. 12d represent the SEM fractography images of samples printed using a $VED=135 \text{ J/mm}^3$ (A-50). Although the flat surfaces and the presence of cleavage planes and ridges were observed and confirm the overall brittle behavior of the samples printed using a high $VED \geq 50 \text{ J/mm}^3$, some local areas have dimples which are characteristics of a ductile fracture. Conversely, the fractography analysis of samples printed with a lower $VED \leq 30 \text{ J/mm}^3$ (F-50) reveals uneven surfaces and a lot of dimples (Fig. 12e) correlated with a ductile behavior. The SEM images allowed to observe unmelted particles trapped inside the pores, some of them being deformed during the compression tests (Fig. 12e).

Fig. 13a shows that the higher the VED, the higher the YS, the lower the strain to failure. Among all the samples, those printed with VED = 135 J/mm³, i.e., with printed densities >99.8 % and heterogeneous α' + β microstructures (Fig. 8a and Fig. 9b,d,f) had YS values ranging from 900 to 1570 MPa, with strains to failure approaching 6-8 %. The B-set samples ($VED = 100 \text{ J/mm}^3$) with fully α '' microstructures and even higher densities (>99.9 %) manifested a similar lack of ductility as their A-set counterparts, but YS values systematically exceeding 1000 MPa. For these two high VED sets, the YS values decrease with an increase in hatching space (Fig. 13b). For the remaining fully α ' martensite samples $(VED \le 50 \text{ J/mm}^3)$, the YS values were systematically lower than 1000 MPa, but showed an inverse trend: they increase with an increase in hatching space (Fig. 13b). To summarize, the microhardness measurements and compression tests revealed that overall, the higher the VED, the higher the hardness and strength of the material, and the lower its ductility.

4. Discussion

4.1. Influence of VED and hatching space on the as-built microstructure

This study established a correlation between the printing parameters and the as-built microstructure of the LPBF-processed Ti62246 alloy. A combination of high *VED* and small h values (high scanning speeds) promoted the formation of hexagonal α' martensite dispersed within the β phase matrix, while the use of opposite conditions (low *VED*, high h, and low scanning speeds) promoted the formation of orthorhombic α'' martensite, commonly observed in the LPBF Ti6246 and other $\alpha + \beta$



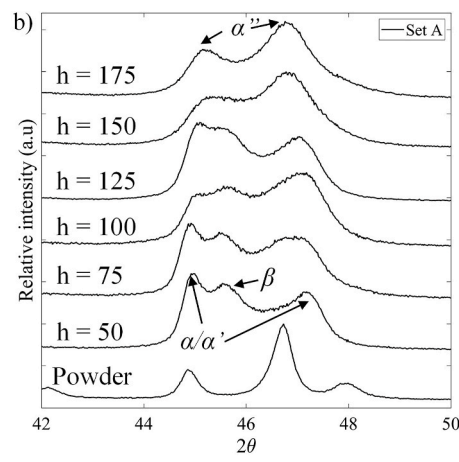


Fig. 8. Microstructural evolution observed through XRD diffractograms depending on a) the parameter sets (VED-BR) with constant h value ($h = 50 \mu m$) and b) the h value at a constant VED-BR parameter set (set A).

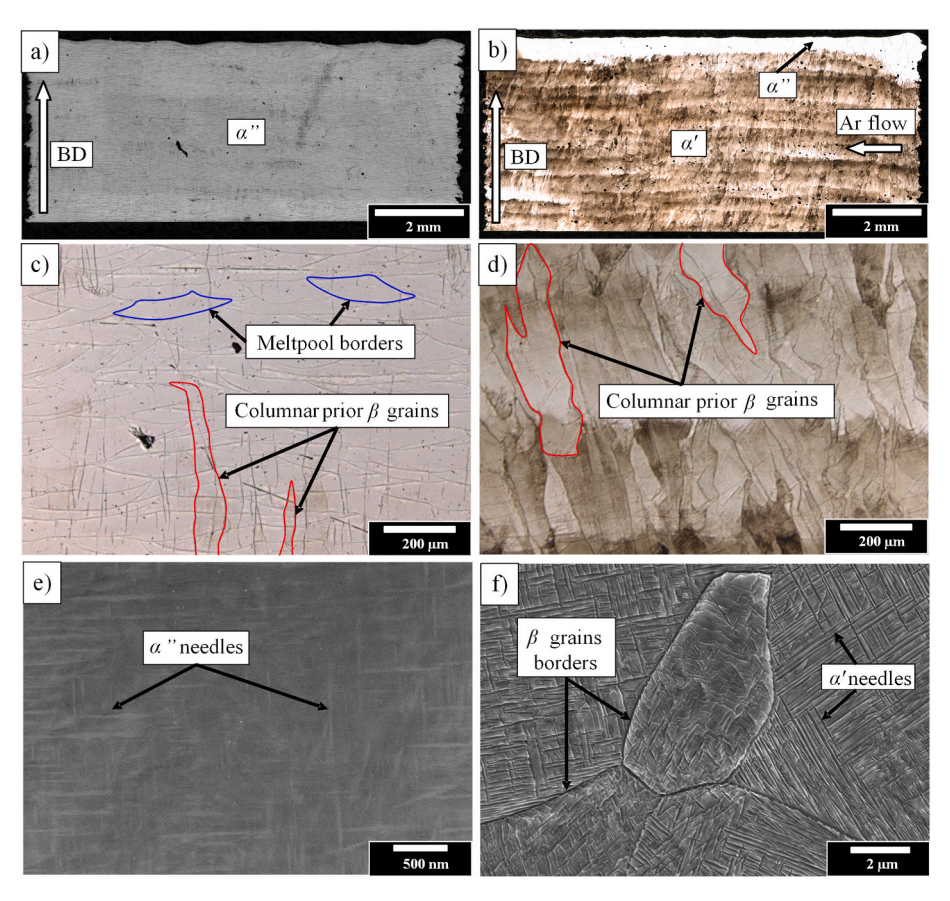


Fig. 9. Observations with confocal microscope (a, b, c, d) and SEM (e, f) of (a, c, e) sample with the as-built α ' martensite microstructure (B-150) and (b, d, f) heterogeneous sample with α' and β phases (A-50).

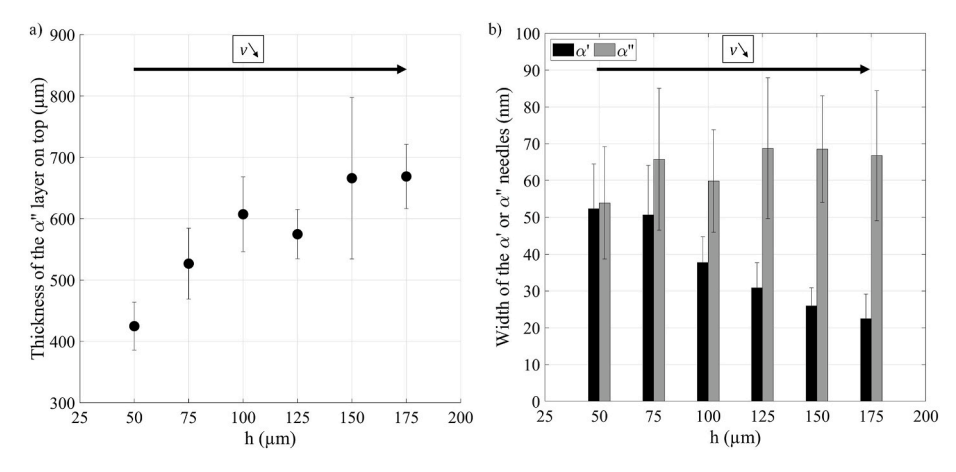


Fig. 10. a) Thickness of the α '' layer on the top surface of heterogeneous samples (set A) depending on the h ratio. b) Needle widths of α' and α' ' martensite as functions of the h value (set A).

titanium alloys with a high β stabilizers content (Fig. 8). Both types of martensite were also reported in LPBF-processed titanium alloys where the α '' martensite is normally not expected, as in near- α Ti6242S [50] or $\alpha+\beta$ Ti64 [51]. The authors attributed such a microstructure evolution to the thermal history of samples and their respective cooling rates which are notably influenced by printing parameters. The highest cooling rates (\sim 10⁸ K/s) were associated with the formation of orthorhombic α '' martensite, while the lowest cooling rates (<10⁶ K/s) were associated with the formation of hexagonal α ' martensite.

In the present study, the fused material thermal history was related to the overlapping ratio W/h, which corresponds to the width of an

experimentally measured single track W (section 3.1), divided by the distance between two consecutive tracks (hatching space h). This value allows to estimate the number of times N (8) each solidified track is exposed to the laser energy input. Additionally, the relative width R% of a solidified track remelted by the next laser pass can be estimated using equation (9).

$$N = \frac{W}{h} - 1 \tag{8}$$

$$R\% = \frac{W - h}{W} * 100 \tag{9}$$

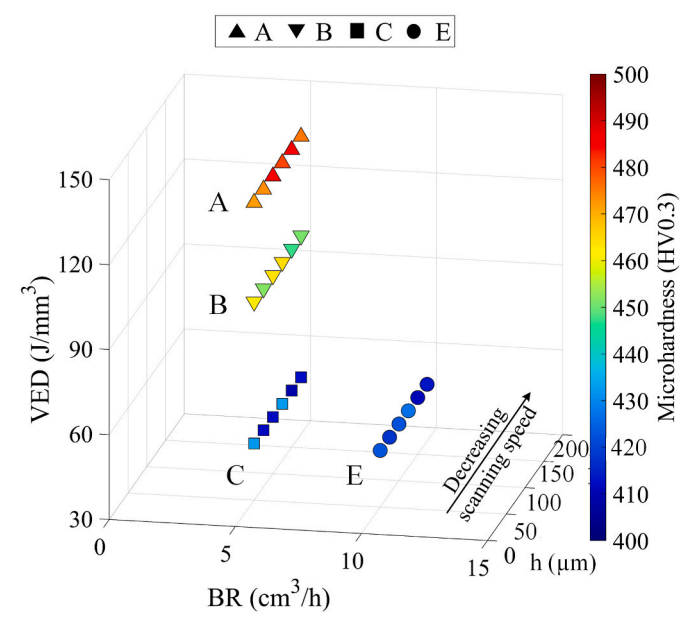


Fig. 11. Evolution of the microhardness measured for the parameter sets A, B, C and E in the VED-BR-h space.

For example, for the parameter set A-125, the melt pool width corresponds to \sim 350 µm (Table 2), which, considering h=125 µm, gives the overlapping ratio W/h=2.8, indicating that during printing, the solidified track will be partially remelted during the next 2 laser passes (N=1.8, Table 3). This parameter set has a remelting fraction of R=64%, meaning that each laser pass generates a melt pool that remelts more than half of a previously solidified track (Fig. 14).

It can be observed from Table 3 that increasing the *VED* value while keeping the *h* value constant increases the *N* value since a higher energy input generates a wider melt pool. This trend is consistent with the results of the single tracks analysis (Fig. 4d). Similarly, for a fixed *VED*, increasing *h* (i.e., reducing speed) results in wider melt pools with lower overlaps *N* and therefore lower remelting proportion *R%*. Overall, for the lowest *VED* (sets C-I), *N* varies from 0 to 1, while the two highest *VED* (A, B) generate the widest melt pools with *N* ranging from 1 to 3.7 and *R* %, varying from \sim 50 to 80 %, thus minimizing the occurrence of lack-of-fusion defects but increasing the probability of keyhole pores formation.

Increasing the melt pool overlaps leads to the already solidified matter receiving an additional energy input, which partially remelts the previously solidified track, slows down cooling of a repeatedly melted alloy, thermally affects (heat affected zone, HAZ) the solidified alloy and thus potentially induces transformations towards the stable phases ($\alpha + \beta$). The literature reports various mechanisms for the decomposition of α " phase depending on the titanium alloy chemical composition and the decomposition temperature. For example, for alloys with high

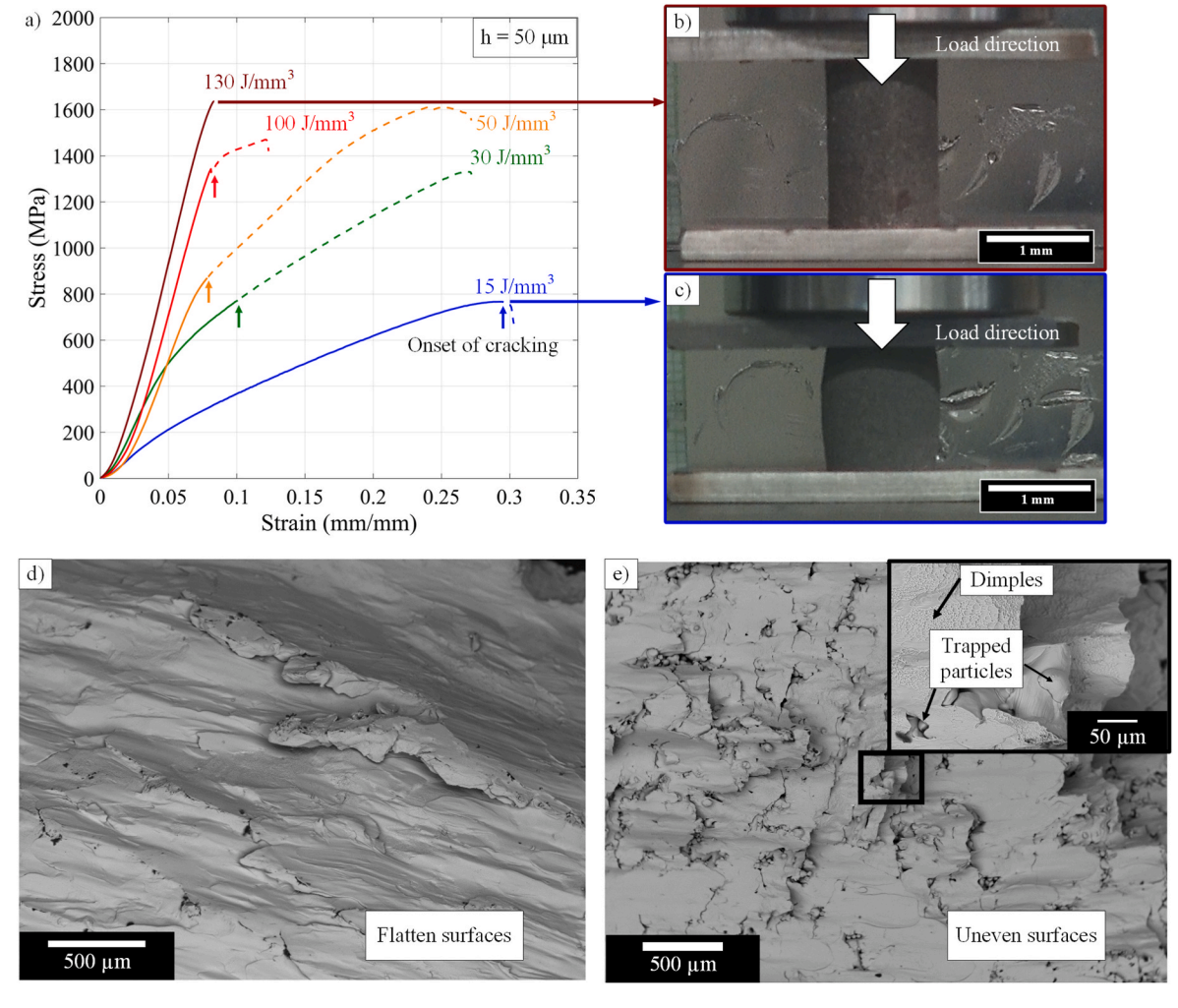


Fig. 12. a) The representative compression stress-strain diagrams (A-50, B-50, E-50, D-50, H-50). The dashed lines correspond to data obtained after detecting an acoustic signal that indicates the onset of cracking identified by an arrow; Photo of the sample at the onset of cracking b) A-50, c) H-50, SEM fractographies: d) A-50 with "brittle" fracture, e) F-50 with "ductile" fracture.

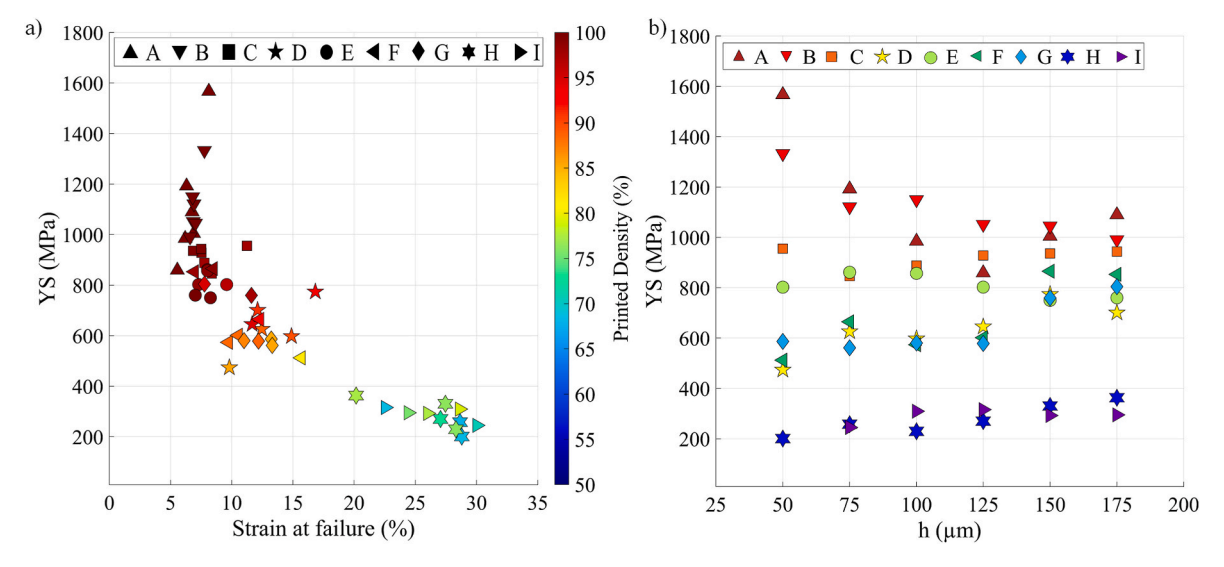


Fig. 13. a) YS at 0.2 % offset versus strain at failure. The relative printed density of the samples is presented in color; b) YS at 0.2 % offset in function of the hatching space.

Table 3
Evolution of the calculated overlap value (N) as a function of the VED and h variations.

Set	VED (J/	h (μm)														175			
	mm ³)	50			75			100			125			150	150 175				
		ν (mm/ s)	N	R %	ν (mm/ s)	N	R %	v (mm/ s)	N	R %	ν (mm/ s)	N	R %	ν (mm/ s)	N	R %	ν (mm/ s)	N	R %
A	135	557	3.7	79	370	2.5	72	278	2.1	67	222	1.8	64	185	1.4	59	159	1.3	57
В	100		2.8	74		2.0	66		1.5	60		1.3	56		1.0	49		1.1	51
C	50		1.5	60		1.2	55		0.7	39		0.4	27		0.3	21		0.3	20
D	30		0.7	42		0.6	38		0.2	16		0.0	0		0	0		0	0
E	50	1111	1.7	63	741	1.3	57	556	0.8	43	444	0.6	36	370	0.5	35	317	0.4	30
F	30		0.9	49		0.8	46		0.4	27		0.2	14		0.0	3		0.0	2
G	30	1667	1.0	50	1111	1.0	50	833	0.4	28	667	0.2	18	556	0.1	9	476	0.0	1
Н	15		1.3	56		0.4	31		0	0		0	0		0	0		0	0
I	15	/	/		2222	0.3	24	1667	0	0	1333	0	0	1111	0	0	952	0	0

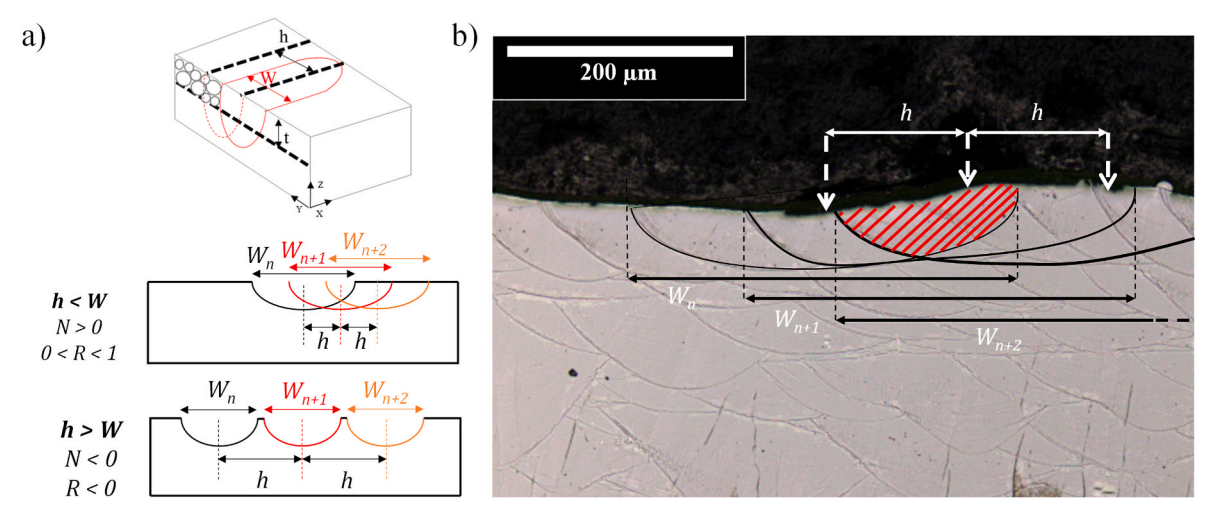


Fig. 14. a) Schematic drawing of the melt pool and different associated metrics. Representation of the h < W case with overlaps and of the h > W case without overlaps, b) optical observations of the melt pools overlapping in sample A-125. The hatched zone is remelted two times (N = 1.8).

proportions of β stabilizers (e.g., Ti-Mo, Ti-Nb, etc.), spinodal decomposition of the initial α '' phase into two rich and lean (in β elements) α '' phases, was reported in Ref. [52]. That study suggests the occurrence of path (10), which starts from the precipitation of metastable $\beta_{\rm M}$ phase

from martensitic α'' phase, followed by the transformation of α''_{lean} phase into α' phase and finally, into α phase [31].

$$\alpha'' \rightarrow \alpha''_{lean} + \beta_M \rightarrow \alpha' + \beta_M \rightarrow \alpha + \beta$$
 (10)

Note, however, that the large melt pool overlaps of the present study were not systematically correlated with the occurrence of in-situ solid state phase transformations. For example, despite their equivalent overlap values ($N \approx 1.5$, Table 3), C-50 and A-150 parameter sets have dissimilar microstructures, respectively α '' and $\alpha' + \beta$. This difference is mainly due to the level of laser energy (VED) used. The partially transformed microstructure was predominantly present in the samples printed with a high VED (>100 J/mm³) and a small hatching space h. In these samples, a combination of the high energy inputs with significant overlaps led to a reduction of the cooling rate, and finally, the formation of partially transformed ($\alpha' + \beta$) microstructures.

The presence of an orthorhombic α " martensite layer (Fig. 10a) in the upper part of the specimens printed with the highest VED (set A, 135 J/mm³) can be justified by the thermal gradient evolution in the process. At the end of the printing of cylindrical samples, final layers contained letters used for sample identification. Therefore, the melted surface areas were significantly smaller than that of an entire cross-section of the cylinder, leading to higher cooling rates and inducing the formation of orthorhombic α " martensite rather than hexagonal α martensite. This assessment is consistent with the evolution of the α '' layer thickness on top of the samples printed with the parameter set A (Fig. 10a). In these samples, when the hatching space h increases, N is reduced (Table 3) and the cooling rate increases, leading to thicker α " layers. The validity of this attribution is reinforced by the presence of α'' martensitecontaining zones on lateral sides of the cylindrical samples (Fig. 15a,b, e.g., A-50 and B-50). These areas were directly exposed to argon flow, and thus to higher thermal gradients. Therefore, the present study indicates that the as-built microstructure of printed samples depends on the thermal history of molten material and can be affected by any factor impacting the samples' temperature, including the number of simultaneously printed samples, the presence or absence of a preheated baseplate, etc.

To the best of the authors' knowledge, among all the studies on LPBF processing of Ti6246 alloys, *Cobbinah* et al. were the only ones to report the formation of $\alpha/\alpha' + \beta$ phase mixtures in the as-built material, and that, regardless of the printing parameters used [40]. The authors did not provide explanations for the appearance of these mixtures instead of the commonly observed α' martensite [34,39]. However, considering that powders used in *Cobbinah* et al. study had a lower content of β -stabilizing molybdenum (5.14 wt%) than reported in the majority of publications (5.5 < wt.% < 6.5), it can be hypothesized that this fact favorized the formation of the mixed microstructures.

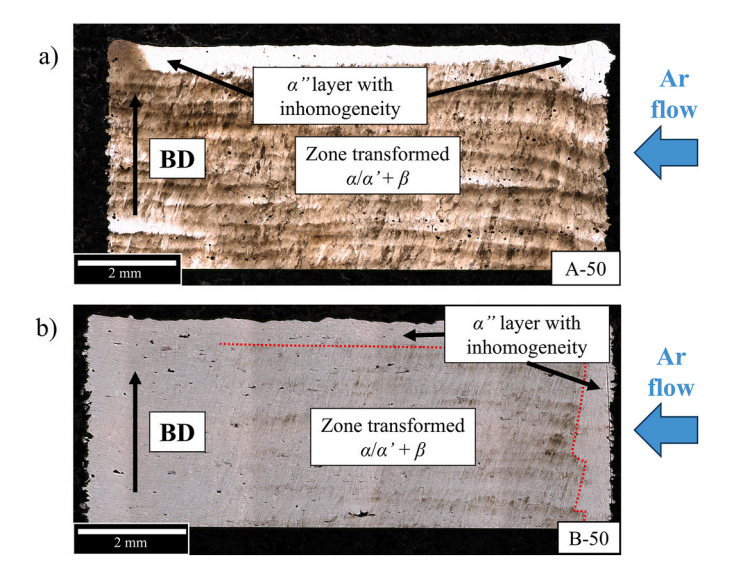


Fig. 15. Cross-section of printed samples with partial and inhomogeneous transformation toward stable phase: a) A-50 and b) B-50.

Note also that very fine (\approx 50 nm) α '' needles observed in the present work have not been systematically reported. While *Peng* et al. described a similar nanostructure [41], *Carrozza* et al. observed much thicker α '' needles (\approx 550–700 nm) [34]. This discrepancy can be attributed to the use in the latter study of a preheated (T = 100 °C) baseplate which reduced the overall cooling rate, thus favoring the formation of coarser martensite needles.

4.2. Printability of the Ti6246 alloy: minimizing the risk of lack-of-fusion defects

The number of studies on the LPBF printability of Ti6246 alloys is limited as compared to the more common Ti64, and the results reported vary significantly. For example, *Hassanin* et al. [39] printed high-density (98.8–99.9 %) Ti6246 samples using a wide range of volumetric energy densities (40 < VED < 160 J/mm³), while *Carrozza* et al. [34] succeeded in printing samples with comparable densities using relatively lower *VED* values of 40–60 J/mm³. In the present study, such low *VED* (50 J/mm³ of the parameter sets C and E) led to the printing of samples with a significant porosity (98–99 %) and a high number of lack-of-fusion defects. Considering our printer configuration, only the use of $VED \geq 100 \, \text{J/mm}^3$ (parameter set B) allowed to print >99.9 % density samples. Multiple reasons are susceptible to explain discrepancies with the aforementioned studies including the use of printers with different laser beam size and preheated baseplates, which would modify the level of heat input needed to melt the material.

Using the *LED* and *VED* thresholds, respectively 0.2 J/mm and 100 J/mm³, allows to establish another process condition in term of the hatching space h value. To print dense samples using a layer thickness $t=50~\mu\text{m}$, h must be bigger than 40 μm (see equations (4) and (7)). Below this hatching space value, the resulting scanning speed v becomes too high (>550 mm/s) to form continuous tracks according to the results of single-track experiments summarized in Fig. 4d. Indeed, defects, such as irregular or partially melted tracks, were reported for most of the single tracks printed using greater scanning speeds.

4.3. Remelting phenomenon and keyhole formation

The multiple exposures caused by the previously described overlapping factor can be correlated with the keyhole porosity observed (Fig. 6af and Fig. 7a). Indeed, samples printed with the highest *VED* generated significant melt pool overlaps (set A, N=1.3 to 3.7 and R%=50-80%) and were at risk of forming keyhole pores. These printing conditions combined high laser powers (P>180 W), low scanning speeds (v<550 mm/s) and therefore, high overlaps (N>1.3). *Carrozza* et al. [34] also reported a higher proportion of circular pores in the case of a very high laser power (P=190 W), which is close to that of the A-set of this study (P=188 W). The present study revealed that using higher hatching distances h reduces the overlaps and decreases the overall temperature in the vicinity of a melt pool, thus reducing the probability of keyhole formation and increasing the printed density from 99.84 (A-75) to 99.99% (A-175), Table A.1 in the appendix).

4.4. Relationship between microstructure and mechanical properties

As observed in the present study, the higher the *VED*, the greater the hardness of as-printed Ti6246 samples. The same tendency can be observed elsewhere, as plotted in Fig. 16a. However, for equivalent *VED* values, the reported microhardness values differ. For example, for *VED* = 50 J/mm³, some authors reported microhardness values close to 350 HV [34,39] while for the same *VED*, *Cobbinah* et al. [40] and the authors of the present study obtained values closer to 435 HV. Such discrepancies can be explained by the differences in printing conditions in terms of powder composition, baseplate temperature, scanning strategy, etc.., affecting the nature and morphology of phases present in the material.

Overall, the lowest microhardness values were reported for samples

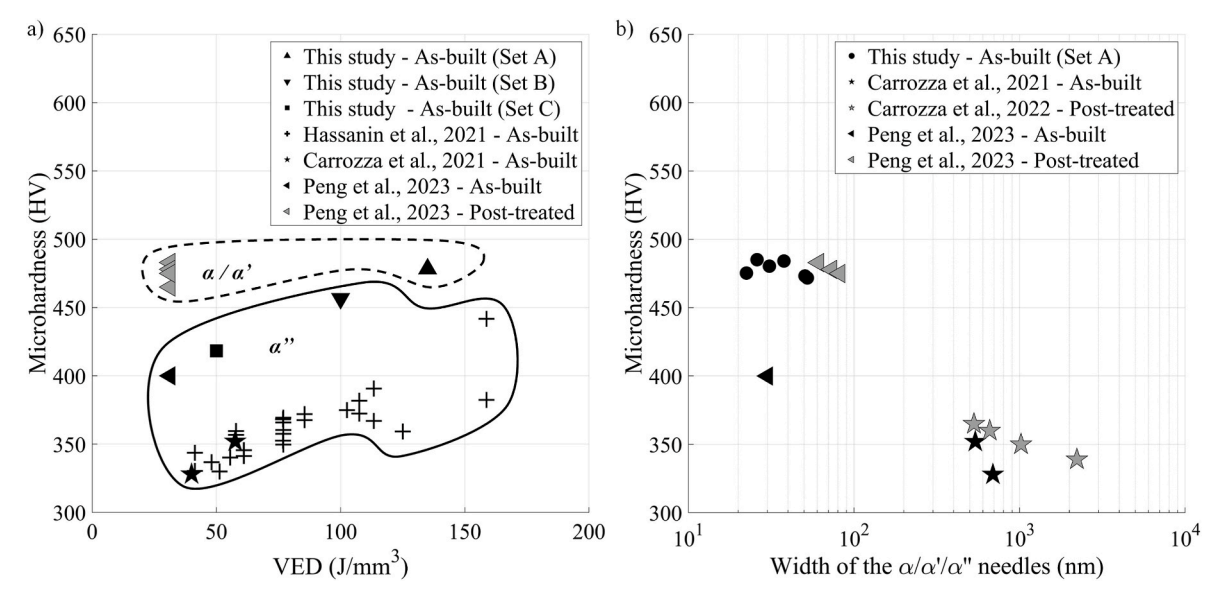


Fig. 16. Evolution of the microhardness values reported in literature [34,39–41] depending on a) the VED and b) the width of the α''/α' martensite needles or the α grains.

having an orthorhombic α '' martensite microstructure with relatively thick needles [34], while the highest values were obtained for samples with a partial or complete transformation towards a stable $\alpha+\beta$ microstructure [40]. Orthorhombic α '' martensite is well known for its softening effect caused by its specific crystal structure and associated slip system, making it more sensitive to plastic deformation [49]. Conversely, the presence of hexagonal α ' martensite strengthens the material and reduces its ductility [53]. These statements are consistent with the generally recommended strategy of post-treating the LPBF-processed Ti6246 alloy to initiate α " $\rightarrow \alpha+\beta$ phase transformation and increase the material hardness [37,39,41]. For example, *Peng* et al., in a bid to maximize the material hardness for tribological applications [41], varied the post-LPBF ageing time and temperature, and established a direct correlation between the hardness values and the width of α laths (11)

$$HV = HV_0 + Kd^{-0.5} (11)$$

where HV is the Vickers hardness; HV_0 , the intrinsic hardness of Ti6246 (424 HVN); K, the Hall-Petch constant (461 VHN.nm $^{-0.5}$), and d, the α laths width.

Note that the partially transformed A-set samples with a narrow hatching space h (Fig. 9b,d,f) manifested an ultra-high hardness close to that of the above-referenced Peng et al. study with alternating thin α and β laths (respectively 35 and 5 nm in width). To support this point, Fig. 16b plots the microhardness values measured in the present study as a function of the $\alpha/\alpha'/\alpha''$ needle size and compares them to those reported in the literature, where it clearly appears that the thinner the needles, the higher the microhardness.

As far as the others mechanical properties are concerned, this study showed that an increase in *VED* leads to an increase in strength at the expense of ductility. To support this observation, we must once again refer to *Carrozza* et al. [34], the only authors to have carried out mechanical testing of this material in the as-built state. They obtained significantly lower strength (YS \approx 450–600 MPa), but much higher ductility (>25 %) characteristics than those in the present study (YS \approx 1000–1600 MPa and \leq 8 %). Note, however, that not only were the testing modes used in the reference and present studies different (tension versus compression), the microstructures of the samples tested were also significantly different: coarse 550–700 nm α " martensite laths in the former case as compared to 50–70 nm α " martensite laths in the

latter case.

That notwithstanding, to provide a necessary balance between the strength and ductility characteristics of an LPBF Ti6246 alloy, the asbuilt alloy must be post-treated with the objective of transforming the as-built α " or mixed α ' + β structure into an equilibrium α + β structure [37].

5. Conclusion

In this study, a wide range of process parameters were applied to print Ti6246 alloy using a limited laser-power system ($P_{\text{max}} = 200 \text{ W}$) without a preheated baseplate. During the printing of single tracks, a minimum linear energy density (LED) of 0.2 J/mm was necessary to guarantee their uniformity, while during full parts printing, an optimized volumetric energy density (VED) of ~100 J/mm³ allowed to minimize defect formation and obtain highly dense parts (>99.9 %). Below this value, wide and irregular lack-of-fusion defects were systematically observed, while over it, the detected pores were small and circular, corresponding to keyhole pores. Overall, the printing parameter set B (volumetric energy density $VED = 100 \text{ J/mm}^3$, build rate BR =5 cm³/h) led systematically to as-built samples with mainly an orthorhombic α '' martensite microstructure, manifesting high ultimate compressive strength (UCS >1000 MPa) but a low strain to failure ($\delta \sim$ 6–8 %). Therefore, the printing parameter sets B with hatching space h > 150 µm (B-150 and B-175) was retained as the best to provide a combination of high mechanical properties and homogeneous initial asbuilt microstructures.

For the process parameters set A with the highest volumetric energy density ($VED=135\,$ J/mm³), partial in situ transformation from α ' martensite towards a mixture of stable $\alpha+\beta$ phases was reported. The transformed $\alpha/\alpha'+\beta$ microstructure induced a slight increase in the mechanical properties (microhardness HV0.3 and yield strength YS), without changing the material ductility. This phase transformation was attributed to a high level of laser power ($P=188\,$ W) combined with a small hatching space h. This combination resulted in multiple laser overlaps (N) and to a large fraction of the remelted material (R%) between each pass, decreasing the cooling rate of the solidified matter and affecting the as-built alloy microstructure.

An accurate control of the microstructure during the printing process is complicated by the fact that the cooling rate can be significantly affected by the baseplate configuration and how the printed part is exposed to gas flow. Furthermore, the identified transformed phases remain metastable, meaning that a subsequent heat treatment is mandatory to create the microstructure suitable for application. The occurrence of these in situ transformations can be beneficially used to tailor specific microstructures in printed parts by optimizing the printing parameters (especially using a double exposure system) and post-process conditions.

CRediT authorship contribution statement

Thibault Mouret: Writing – original draft, Visualization, Software, Methodology, Investigation, Formal analysis, Data curation, Conceptualization. **Aurore Leclercq:** Writing – original draft, Visualization, Validation, Software, Methodology, Investigation, Formal analysis, Data curation. **Vladimir Brailovski:** Writing – review & editing,

Visualization, Validation, Supervision, Resources, Project administration, Methodology, Funding acquisition, Conceptualization.

Declaration of competing interest

The authors declare that they have no known competing financial interests or personal relationships that could have appeared to influence the work reported in this paper.

Acknowledgments

The authors acknowledge the financial support provided by CRIAQ (Consortium de Recherche et d'Innovation en Aérospatiale au Québec) in the framework of the Exploring Innovation – INNOV-R program, NSERC (Natural Sciences and Engineering Research Council of Canada) and Exonetik Turbo inc.

Appendix

Table A.1
Printed specimens nomenclature, plan of experiments, μCT density, yield strength at 0.2 % offset, ultimate compression strength, stain to failure, microhardness.

Name	Hatching space (µm)	Power (W)	Scanning speed (v)	Volumetric Energy Density (J/mm ³)	Build Rate (cm ³ /h)	Density μCT (%)	YS at 0.2 % (MPa)	UCS (MPa)	δ (%)	HV (HV0.3)
A-50	50	188	556	135	5	99.91	1567	1636	8	472 ± 1
B-50	00	139	556	100	5	99.96	1333	1343	8	461 ± 9
C-50		69	556	50	5	97.77	955	1242	11	432 ± 1
D-50		42	556	30	5	85.49	474	773	10	x
E-50		139	1111	50	10	96.51	802	1013	10	423 ± 1
F-50		83	1111	30	10	81.42	512	1013	16	x
G-50		125	1667	30	15	85.31	587	1016	13	x
H-50		63	1667	15	15	68.49	201	767	29	x
A-75	75	188	370	135	5	99.84	1193	1193	6	473 ± 1
л-75 В-75	73	139	370	100	5	99.99	1122	1122	7	473 ± 1 452 ± 2
C-75		69	370	50	5	98.42	846	966	8	432 ± 2 412 ± 2
C-75 D-75		42	370 370	30	5 5	98.42 88.67	626	900	8 12	
		139	741	50	10	98.66	861	1024	8	x 418 ± 13
E-75				30		92.68	665	1122	8 12	
F-75		83	741	30	10					x
G-75		125	1111		15	85.54	561	1033	13	x
H-75		63	1111	15	15	67.81	258	997	29	x
I-75	100	125	2222	15	30	70.84	245	969	30	<i>x</i>
A-100	100	188	278	135	5	99.79	985	985	6	484 ± 1
B-100		139	278	100	5	99.99	1150	1150	7	464 ± 2
C-100		69	278	50	5	97.72	888	1048	8	412 ± 2
D-100		42	278	30	5	89.48	598	1085	15	x
E-100		139	556	50	10	98.94	857	979	8	423 ± 1
F-100		83	556	30	10	88.32	574	864	10	x
G-100		125	833	30	15	86.95	580	917	11	x
H-100		63	833	15	15	76.10	230	875	28	x
I-100		125	1667	15	30	79.00	309	1078	29	x
A-125	125	188	222	135	5	99.83	859	859	6	480 ± 1
B-125		139	222	100	5	100.00	1051	1051	7	464 ± 3
C-125		69	222	50	5	98.84	928	1056	8	433 ± 1
D-125		42	222	30	5	94.70	645	1054	12	x
E - 125		139	444	50	10	98.49	802	870	7	427 ± 1
F-125		83	444	30	10	88.40	602	929	11	x
G-125		125	667	30	15	88.57	578	956	12	x
H-125		63	667	15	15	73.18	270	920	27	x
I-125		125	1333	15	30	68.61	316	920	23	x
A-150	150	188	185	135	5	99.96	1004	1004	7	485 ± 1
B-150		139	185	100	5	99.98	1045	1045	7	447 ± 3
C-150		69	185	50	5	99.58	936	1026	7	409 ± 3
D-150		42	185	30	5	92.77	774	1264	17	x
E-150		139	370	50	10	99.55	750	902	8	411 ± 8
F-150		83	370	30	10	98.89	865	1046	8	x
G-150		125	556	30	15	97.53	759	1194	12	x
H-150		63	556	15	15	76.20	330	972	27	x
I-150		125	1111	15	30	77.45	292	923	26	x
A-175	175	188	159	135	5	99.99	1090	1090	7	475 ± 1
B-175		139	159	100	5	99.99	991	991	7	451 ± 4

(continued on next page)

Table A.1 (continued)

Name	Hatching space (μm)	Power (W)	Scanning speed (v)	Volumetric Energy Density (J/mm³)	Build Rate (cm ³ /h)	Density μCT (%)	YS at 0.2 % (MPa)	UCS (MPa)	δ (%)	HV (HV0.3)
C-175		69	159	50	5	99.41	943	1094	8	412 ± 12
D-175		42	159	30	5	90.89	701	1084	12	x
E - 175		139	317	50	10	99.95	760	840	7	413 ± 22
F-175		83	317	30	10	98.09	853	853	7	x
G-175		125	476	30	15	94.86	804	956	8	x
H-175		63	476	15	15	77.32	363	849	20	x
I-175		125	952	15	30	75.49	295	856	24	x

x: microhardness measurements were not performed due to density < 95%.

Data availability

Data are contained within the article.

References

- S.A.M. Tofail, E.P. Koumoulos, A. Bandyopadhyay, S. Bose, L. O'Donoghue, C. Charitidis, Additive manufacturing: scientific and technological challenges, market uptake and opportunities, Mater. Today 21 (1) (Jan. 2018) 22–37, https://doi.org/10.1016/j.mattod.2017.07.001.
- [2] M. Javaid, A. Haleem, R.P. Singh, R. Suman, S. Rab, Role of additive manufacturing applications towards environmental sustainability, Adv. Ind. Eng. Polym. Res. 4 (4) (Oct. 2021) 312–322, https://doi.org/10.1016/j. aiepr.2021.07.005.
- [3] D.D. Gu, W. Meiners, K. Wissenbach, R. Poprawe, Laser additive manufacturing of metallic components: materials, processes and mechanisms, Int. Mater. Rev. 57 (3) (May 2012) 133–164. https://doi.org/10.1179/1743280411Y.0000000014.
- [4] A. Hemmasian Ettefagh, S. Guo, J. Raush, Corrosion performance of additively manufactured stainless steel parts: a review, Addit. Manuf. 37 (Jan. 2021) 101689, https://doi.org/10.1016/j.addma.2020.101689.
- [5] S. Sanchez, et al., Powder bed fusion of nickel-based superalloys: a review, Int. J. Mach. Tool Manufact. 165 (Jun. 2021) 103729, https://doi.org/10.1016/j. ijmachtools.2021.103729.
- [6] S.K. Sharma, et al., Advancements in the additive manufacturing of magnesium and aluminum alloys through laser-based approach, Materials 15 (22) (Jan. 2022) 22, https://doi.org/10.3390/ma15228122.
- [7] A. Leclercq, V. Brailovski, Improving laser powder bed fusion printability of tungsten powders using simulation-driven process optimization algorithms, Materials 17 (8) (Jan. 2024) 8, https://doi.org/10.3390/ma17081865.
- [8] D. Schimbäck, J. Braun, G. Leichtfried, H. Clemens, S. Mayer, Laser powder bed fusion of an engineering intermetallic TiAl alloy, Mater. Des. 201 (Mar. 2021) 109506, https://doi.org/10.1016/j.matdes.2021.109506.
- [9] A.G. Illarionov, et al., A review—Additive manufacturing of Intermetallic alloys based on orthorhombic titanium aluminide Ti2AlNb, Materials 16 (3) (Jan. 2023) 991, https://doi.org/10.3390/ma16030991.
- [10] S. Cao, Y. Zou, C.V.S. Lim, X. Wu, Review of laser powder bed fusion (LPBF) fabricated Ti-6Al-4V: process, post-process treatment, microstructure, and property, Light Adv. Manuf. 2 (3) (Sep. 2021) 313–332, https://doi.org/10.37188/lam.2021.020.
- [11] F. Bartolomeu, M. Gasik, F.S. Silva, G. Miranda, Mechanical properties of Ti6Al4V fabricated by laser powder bed fusion: a review focused on the processing and microstructural parameters influence on the final properties, Metals 12 (6) (Jun. 2022) 6, https://doi.org/10.3390/met12060986.
- [12] R. Boyer, G. Welsch, E.W. Collings (Eds.), Materials Properties Handbook: Titanium Alloys, 4. Printing, ASM International, Materials Park, Ohio, 2007.
- [13] X. Yang, W. Ma, Z. Zhang, S. Liu, H. Tang, Ultra-high specific strength Ti6Al4V alloy lattice material manufactured via selective laser melting, Mater. Sci. Eng. A 840 (Apr. 2022) 142956, https://doi.org/10.1016/j.msea.2022.142956.
- [14] A.M. Khorasani, M. Goldberg, E.H. Doeven, G. Littlefair, Titanium in biomedical applications—Properties and fabrication: a review, J. Biomater. Tissue Eng. 5 (8) (Aug. 2015) 593–619, https://doi.org/10.1166/jbt.2015.1361.
- [15] J. Dias Corpa Tardelli, C. Bolfarini, A. Cândido dos Reis, Comparative analysis of corrosion resistance between beta titanium and Ti-6Al-4V alloys: a systematic review, J. Trace Elem. Med. Biol. 62 (Dec. 2020) 126618, https://doi.org/ 10.1016/j.jtemb.2020.126618.
- [16] J.D. Destefani, Introduction to titanium and titanium alloys, in: Properties and Selection: Nonferrous Alloys and Special-Purpose Materials, ASM Handbook Committee, ASM International, 1990, pp. 586–591, https://doi.org/10.31399/ asm.bb.v02.a0001080.
- [17] E.O. Ezugwu, Z.M. Wang, Titanium alloys and their machinability—a review, J. Mater. Process. Technol. 68 (3) (Aug. 1997) 262–274, https://doi.org/10.1016/ S0924-0136(96)00030-1.
- [18] V.M. Tabie, C. Li, W. Saifu, J. Li, X. Xu, Mechanical properties of near alpha titanium alloys for high-temperature applications - a review, Aircraft Eng. Aero. Technol. 92 (4) (Mar. 2020) 521–540, https://doi.org/10.1108/AEAT-04-2019-0086.

- [19] I. Weiss, S.L. Semiatin, Thermomechanical processing of alpha titanium alloys—an overview, Mater. Sci. Eng. A 263 (2) (May 1999) 243–256, https://doi.org/ 10.1016/S0921-5093(98)01155-1.
- [20] P. Yadav, K.K. Saxena, Effect of heat-treatment on microstructure and mechanical properties of Ti alloys: an overview, Mater. Today Proc. 26 (Jan. 2020) 2546–2557, https://doi.org/10.1016/j.matpr.2020.02.541.
- [21] B. Jin, et al., A review of additive manufacturing techniques and post-processing for high-temperature titanium alloys, Metals 13 (8) (Aug. 2023) 8, https://doi.org/ 10.3390/met13081327.
- [22] J.D. Cotton, et al., State of the art in beta titanium alloys for airframe applications, JOM 67 (6) (Jun. 2015) 1281–1303, https://doi.org/10.1007/s11837-015-1442-4.
- [23] R.P. Kolli, A. Devaraj, A review of metastable beta titanium alloys, Metals 8 (7) (Jul. 2018) 7, https://doi.org/10.3390/met8070506.
- [24] S.R. Soundararajan, et al., Heat treatment of metastable beta titanium alloys, in: Welding - Modern Topics, IntechOpen, 2020, https://doi.org/10.5772/ intechopen.92301.
- [25] H.J. Hucek, Aerospace structural metals handbook: 1989 publication with 1988 supplement XXI incorporated, Columbus, OH 4 (1979).
- [26] B. Meier, F. Warchomicka, J. Petrusa, R. Kaindl, W. Waldhauser, C. Sommitsch, High temperature tensile strength of TI6AL4V processed by L-PBF—Influence of microstructure and heat treatment, BHM Berg- Hüttenmännische Monatsh. 168 (5) (May 2023) 247–253, https://doi.org/10.1007/s00501-023-01346-3.
- [27] M. Evans, A.R. Ward, Corrosion resistance of Ti-6246 for high power aeroengine compressor discs and blades, Mater. Sci. Technol. 17 (8) (Aug. 2001) 945–953, https://doi.org/10.1179/026708301101510771.
- [28] B. Vincent, et al., Comparison between the oxidation behaviors of Ti6242S, Ti6246, TiXT alloys, and pure titanium, Oxid. Metals 96 (3) (Oct. 2021) 283–294, https://doi.org/10.1007/s11085-021-10051-w.
- [29] B. Hargrave, M. Gonzalez, K. Maskos, J. Skogsberg, J. Grauman, Titanium alloy tubing for hpht octg applications, Presented Corrosion (2010). San Antonio, Mar. 2010.
- [30] F.F. Zhang, C. Feng, L.J. Zhu, W.W. Song, Research progress on corrosion resistance of titanium alloy oil well tubing, Mater. Sci. Forum 1035 (Jun. 2021) 528–533. https://doi.org/10.4028/www.scientific.net/MSF.1035.528.
- [31] M. Motyka, Martensite formation and decomposition during traditional and AM processing of two-phase titanium alloys—an overview, Metals 11 (3) (Mar. 2021) 3, https://doi.org/10.3390/met11030481.
- [32] M. Young, E. Levine, H. Margolin, The aging behavior of orthorhombic marten site in Ti-6-2-4-6, Metall. Trans. A 5 (8) (Aug. 1974) 1891–1898, https://doi.org/ 10.1007/BF02644157.
- [33] S. Bein, J. Béchet, Phase transformation kinetics and mechanisms in titanium alloys Ti-6.2.4.6,β-CEZ and Ti-10.2.3, J. Phys. IV 6 (C1) (Jan. 1996) C1–C108, https://doi.org/10.1051/jp4:1996110.
- [34] A. Carrozza, A. Aversa, P. Fino, M. Lombardi, A study on the microstructure and mechanical properties of the Ti-6Al-2Sn-4Zr-6Mo alloy produced via laser powder bed fusion, J. Alloys Compd. 870 (Jul. 2021) 159329, https://doi.org/10.1016/j. jallcom.2021.159329.
- [35] A. Carrozza, B.A. Bircher, A. Aversa, S. Biamino, Investigating complex geometrical features in LPBF-produced parts: a material-based comparison between different titanium alloys, Met. Mater. Int. 29 (12) (Dec. 2023) 3697–3714, https://doi.org/ 10.1007/s12540-023-01460-4.
- [36] A. Aversa, et al., A comparison between the residual stresses of Ti6Al4V and Ti-6Al-2Sn-4Zr-6Mo processed by laser powder bed fusion, Materials 18 (3) (Jan. 2025) 3, https://doi.org/10.3390/ma18030689.
- [37] A. Carrozza, A. Aversa, P. Fino, M. Lombardi, Towards customized heat treatments and mechanical properties in the LPBF-Processed Ti-6Al-2Sn-4Zr-6Mo alloy, Mater. Des. 215 (Mar. 2022) 110512, https://doi.org/10.1016/j.matdes.2022.110512.
- [38] G. Pirro, A. Martucci, A. Morri, M. Lombardi, L. Ceschini, A novel solution treatment and aging for powder bed fusion-laser beam Ti-6Al-2Sn-4Zr-6Mo alloy: microstructural and mechanical characterization, Int. J. Miner. Metall. Mater. 32 (2) (Feb. 2025) 414–424, https://doi.org/10.1007/s12613-024-3006-5.
- [39] H. Hassanin, Y. Zweiri, L. Finet, K. Essa, C. Qiu, M. Attallah, Laser powder bed fusion of Ti-6Al-2Sn-4Zr-6Mo alloy and properties prediction using deep learning approaches, Materials 14 (8) (Jan. 2021) 8, https://doi.org/10.3390/ mal4082056.
- [40] P.V. Cobbinah, et al., Peculiar microstructural evolution and hardness variation depending on laser powder bed fusion-manufacturing condition in Ti-6Al-2Sn-4Zr-6Mo, Smart Mater. Manuf. 2 (Jan. 2024) 100050, https://doi. org/10.1016/j.smmf.2024.100050.

- [41] H. Peng, S. Wu, W.H. Kan, S.C.V. Lim, Y. Zhu, A. Huang, Rapid hardening response of ultra-hard Ti-6Al-2Sn-4Zr-6Mo alloy produced by laser powder bed fusion, Scr. Mater. 226 (Mar. 2023) 115209, https://doi.org/10.1016/j. scriptamat.2022.115209.
- [42] W.H. Kan, H. Peng, S. Lim, Y. Zhu, K. Zhang, A. Huang, The mechanisms behind the tribological behavior of titanium alloys processed by laser powder bed fusion sliding against steel, Tribol. Int. 180 (Feb. 2023) 108279, https://doi.org/10.1016/ j.triboint.2023.108279.
- [43] A. Martucci, L. Iannucci, M. Lombardi, S. Grassini, Effect of microstructural anisotropy and heat treatment on the corrosion behaviour of additively manufactured Ti-6Al-2Sn-4Zr-6Mo alloy, J. Alloys Compd. 1008 (Dec. 2024) 176746, https://doi.org/10.1016/j.jallcom.2024.176746.
- [44] B. Han, M. Marya, An evaluation of the mechanical properties and sulfide stress cracking of additively manufactured alloy Ti-6Al-2Sn-4Zr-6Mo for sour geothermal use. Presented at the CONFERENCE 2025, Association for Materials Protection and Performance, Apr. 2025, pp. 1–15, https://doi.org/10.5006/C2025-00101.
- [45] AMS G Titanium and Refractory Metals Committee, Titanium Alloy Bars, Wire, and Forgings, 6Al - 2Sn - 4Zr - 6Mo, Solution and Precipitation Heat Treated. doi: 10.4271/AMS4981.
- [46] C. Desrosiers, et al., Correlative laser confocal microscopy study and multimodal 2D/3D registration as ground truth for X-ray inspection of internal defects in LPBF manufacturing, E-J. Nondestruct. Test. 27 (3) (Mar. 2022), https://doi.org/ 10.58286/26642.

- [47] J. Lindblad, Surface area estimation of digitized 3D objects using weighted local configurations, Image Vis Comput. 23 (2) (Feb. 2005) 111–122, https://doi.org/ 10.1016/j.imavis.2004.06.012.
- [48] Test Methods of Compression Testing of Metallic Materials at Room Temperature, E9-E9. doi: 10.1520/E0009-09.
- [49] Y. Guo, T. Jung, Y.L. Chiu, H. Li, S. Bray, P. Bowen, Microstructure and microhardness of Ti6246 linear friction weld, Mater. Sci. Eng. A 562 (Feb. 2013) 17–24, https://doi.org/10.1016/j.msea.2012.10.089.
- [50] C. Fleißner-Rieger, et al., On the existence of orthorhombic martensite in a near-α titanium base alloy used for additive manufacturing, J. Alloys Compd. 897 (Mar. 2022) 163155, https://doi.org/10.1016/j.jallcom.2021.163155.
- [51] Z. Xie, Y. Dai, X. Ou, S. Ni, M. Song, Effects of selective laser melting build orientations on the microstructure and tensile performance of Ti-6Al-4V alloy, Mater. Sci. Eng. A 776 (Mar. 2020) 139001, https://doi.org/10.1016/j. msea 2020 139001
- [52] H.M. Flower, R. Davis, D.R.F. West, Martensite formation and decomposition in alloys of titanium containing β-Stabilizing elements, in: J.C. Williams, A.F. Belov (Eds.), Titanium and Titanium Alloys: Scientific and Technological Aspects Volume 3, Springer US, Boston, MA, 1982, pp. 1703–1715, https://doi.org/10.1007/978-1-4757-1758-7
- [53] J. He, et al., The martensitic transformation and mechanical properties of Ti6Al4V prepared via selective laser melting, Materials 12 (2) (Jan. 2019) 2, https://doi.org/10.3390/ma12020321.